Photoinduced band renormalization effects in the topological nodal-line semimetal ZrSiS

Somnath Biswas 0,1,* Ioannis Petrides 0,2,* Robert J. Kirby, 1 Catrina Oberg 0,1 Sebastian Klemenz 0,1 Caroline Weinberg 0,1 Austin Ferrenti, Prineha Narang, 2,† Leslie M. Schoop, 1,‡ and Gregory D. Scholes, and Gregory D. Scholes ¹Department of Chemistry, Princeton University, Princeton, New Jersey 08544, USA ²John A. Paulson School of Engineering and Applied Sciences, Harvard University, Cambridge, Massachusetts 02138, USA

(Received 14 June 2022; revised 30 August 2022; accepted 22 September 2022; published 11 October 2022)

Out-of-equilibrium effects provide an elegant pathway for probing and understanding the underlying physics of topological materials. In particular, controlling electronic band structure properties using ultrafast optical pulses has shown promise for creating exotic states of matter. Of recent interest is band renormalization in Dirac and Weyl semimetals as it leads to direct physical observables through the enhancement of the effective mass or in the shift of resonant energies. Here we provide experimental and theoretical signatures of photoinduced renormalization of the electronic band structure in the topological nodal-line semimetal ZrSiS. Specifically, we show how the change in the transient reflectivity spectra under femtosecond optical excitations is induced by out-of-equilibrium effects that renormalize the kinetic energy of electrons. We associate the observed spectral features with an enhancement of the effective mass and to a redshift of the resonant frequency as a function of pump field strength. Finally, we show that the transient relaxation dynamics of the reflectivity is primarily an electronic effect with a negligible phononic contribution. Our study presents conclusive modifications of electronic properties in ZrSiS using ultrashort pulses and demonstrates the potential of this approach in creating photoinduced phases in topological quantum matter through an all-optical route.

DOI: 10.1103/PhysRevB.106.134303

I. INTRODUCTION

Dirac nodal-line semimetals (NLSMs) of the family ZrSiX, with X = S, Se, or Te, have been the subject of intense research due to the presence of topologically nontrivial states [1–3], unusually large magnetoresistance [4–6], high carrier mobility [7,8], strong Zeeman splitting [9], and frequency-independent optical conductivity [10]. In addition to these remarkable properties, the presence of extended linear band crossings along lines/loops in the Brillouin zone of NLSMs are anticipated to show enhanced correlation effects [11-14]; in fact, quantum oscillations studies of ZrSiS in high external magnetic fields showed an enhancement of the effective mass of the quasiparticles [15]. The ability to manipulate the electronic properties in such a material is therefore a primary driving force towards understanding and discovering new phases of matter [16–18].

Coupling electronic states through ultrafast optical pulses is an elegant way to drastically change macroscopic (for example, electrical or optical) properties of materials [19-21]. Out-of-equilibrium changes can be detected in a pump-probe approach, where a high-frequency external field, or pump, is used to drive the system, while a subsequent weak probe field is used to detect the induced changes [22-24]. For example, ultrafast optical pulses have been shown to significantly alter the structure of Dirac or Weyl nodes by shifting, splitting, merging, or even opening a gap in the energy spectrum [25–30]. In addition to this fundamental physics, the out-of-equilibrium responses of Dirac and Weyl semimetals offer technological advantages, including optical switching in midinfrared lasers [31], broadband infrared photodetectors [32,33], an efficient terahertz source via nonpurturbative nonlinear effects [34,35], and their use in high-frequency optoelectronic devices [31,36–38].

While there are studies on the ultrafast dynamics of ZrSiX NLSMs in which the transient carrier relaxation mechanisms have been discussed [39-41], direct manipulation of the electronic band structure, relaxation times, and mass enhancement via external electromagnetic fields has not been studied before in detail. Recently, time-resolved angle-resolved photoemission spectroscopy measurements in a NLSM (ZrSiSe) and in the quasi-two-dimensional semimetal BaNiS2 have shown that photoexcitation with an optical pulse causes band renormalization within a few hundred femtoseconds [42,43]. Therefore, all-optical control of such effects through the strength of the pump pulse provides an exciting opportunity to explore out-of-equilibrium phenomena as well as the possibility of correlation-driven physics in this class of materials. Furthermore, studying photoinduced band renormalization effects using table-top transient reflectivity measurements lays the foundation for developing a table-top optical setup for understanding and, in particular, controlling quantum matter.

Here, we use broadband visible (1.75-2.25 eV) and near-infrared (0.8-1.4 eV) transient optical reflectively measurements to show the effect of ultrafast optical excitations on the electronic bands, as well as on the electronic relaxation

^{*}These authors contributed equally to this work.

[†]prineha@seas.harvard.edu

[‡]lschoop@princeton.edu

[§]gscholes@princeton.edu

times in ZrSiS. Our results demonstrate the energy shift and mass enhancement of a Lorentzian peak at 2.06 eV within a few hundred femtoseconds following photoexcitation. We additionally observe a decrease in the electronic relaxation rate with pump fluence, in contrast to the observed coherent phonon (A_{1g}) lifetime that remains independent. These findings are well captured within a tight-binding model, where the renormalization of the electronic kinetic energy due to the ultrafast pump pulse leads to the observed changes in reflectivity. Our study combines an out-of-equilibrium approach with a table-top, all-optical experimental platform to demonstrate that band renormalization in ZrSiS is inherently an ultrafast effect that originates from the modification of the electronic spectrum due to the pump field.

II. TIGHT-BINDING DESCRIPTION

In this section we use an out-of-equilibrium formalism to calculate the response of a concrete tight-binding model characterizing the material. We start by calculating the equilibrium density of states and find that the spectrum at particular points in the Brillouin zone is approximated by a quadratic dispersion with well-defined resonant energy, velocity, and effective mass. Next, we include the effect of a high-frequency pump and find that it renormalizes the kinetic energy of the electrons, leading to a change in their dispersion relation. Finally, we determine the relaxation dynamics of such modifications back to their equilibrium values.

The qualitative features of the material are well captured by a two-orbital model [44] composed of a d_{xy} orbital localized on the Zr atoms and a superposition of p_x and p_y orbitals localized on the Si atoms [see Fig. 1(a)]. The resulting tight-binding lattice, shown in Fig. 1(b), has four degrees of freedom per unit cell and is determined by the nearest-and next-nearest-neighbor hopping amplitudes. In a suitable gauge, the Bloch Hamiltonian is given by

$$\hat{H}(k) = d \cdot \gamma, \tag{1}$$

where

$$d = \left\{ \Delta, 2K_1 \sum_{\mu} \cos(k_{\mu}), 4K_2 \prod_{\mu} \sin(k_{\mu}), \right.$$

$$\times 4K_3 \cos(k_x) \sin(k_y) \right\}$$
(2)

is a real-valued vector and

$$\boldsymbol{\gamma} = \{ \sigma_z \otimes \mathbb{1}, \, \sigma_z \otimes \sigma_x, \, \sigma_x \otimes \mathbb{1}, \, \sigma_y \otimes \mathbb{1} \}, \tag{3}$$

are four 4×4 Hermitian matrices. The parameters of the model are determined numerically by projecting the density functional theory eigenstates onto two maximally localized Wannier orbitals [44]. Here, $\Delta = 0.853\,\mathrm{eV}$ is the detuning between the orbitals on the same site, $K_1 = 0.74\,\mathrm{eV}$ is the hopping amplitude between neighboring orbitals of the same type, $K_2 = 0.14\,\mathrm{eV}$ is the next-nearest-neighbor hopping amplitude between inequivalent orbitals, and $K_3 \sim 0$ is the dimerization of the next-nearest-neighbor hopping amplitude. The latter is chosen heuristically to reflect the difference of the overlap

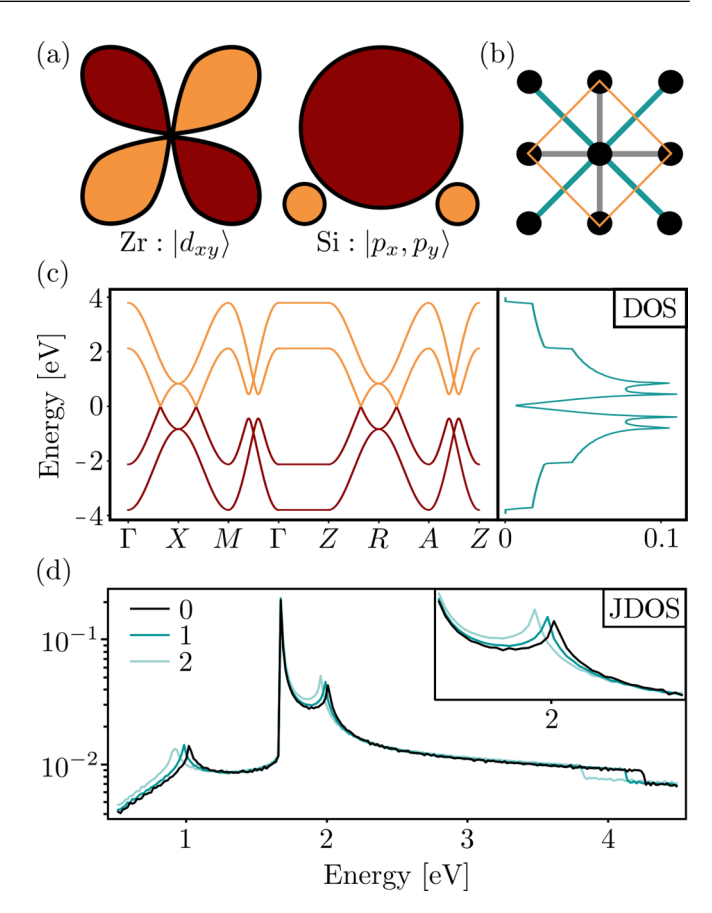


FIG. 1. (a) A schematic of the two orbitals of the effective tight-binding model. Left: The d_{xy} orbital localized on the Zr atoms. Right: The superposition of p_x and p_y orbitals localized on the Si atoms. (b) The square lattice with nearest-neighbor hopping K_1 (gray) between equivalent orbitals and next-nearest-neighbor hopping (turquoise) between inequivalent orbitals; the dimerization parameter K_3 is not shown for simplicity. The unit cell is denoted by the yellow square. (c) The band structure of the model along the high-symmetry points and the local density of states (DOS). (d) The joint density of states (JDOS) of the model on a log-lin scale for three different values of driving strength A_0 .

between next-nearest-neighbor orbitals along the $\hat{x} \pm \hat{y}$ directions [see Fig. 1(a)].

The band structure of this model is composed of four bands at opposite energies that cross the Fermi level at particular points in the Brillouin zone [see Fig. 1(c)]. At higher energies, the spectrum is characterized by a set of saddle points at X (equivalently, at R), as well as a set of band maxima at Γ and M (equivalently, at Z and A). In addition, two minima appear along the $M \to \Gamma$ line (equivalently, $A \to Z$ line). The dispersion relation around these points is well approximated by

$$\mathcal{E} = \mathcal{E}_0 + v_{\mu} k^{\mu} + \frac{1}{2} m_{\mu\nu}^{-1} k^{\mu} k^{\nu}, \tag{4}$$

where \mathcal{E}_0 is the resonant energy, $v_{\mu} = \langle \partial_{k_{\mu}} \hat{H}(k) \rangle$ is the velocity, and $m_{\mu\nu}^{-1} = \langle \partial_{k_{\mu}k_{\nu}}^2 \hat{H}(k) \rangle$ is the effective mass of the associated eigenstate. The local density of states, shown in Fig. 1(c), has the two expected types of singularities: (i) a logarithmic peak $\sim \ln |\mathcal{E}_0 - \omega|$ at $|\mathcal{E}_0| = \Delta$, mainly origi-

nating from the saddle points, and (ii) an abrupt change at $|\mathcal{E}_0| = 4K_1 \pm \Delta$ and $\pm 4K_2$, corresponding to the maxima and minima found in the band structure.

In the out-of-equilibrium case, the high-frequency electromagnetic field representing the pump is incorporated using generalized Peierls substitutions [45–48], where the momentum coordinates k are shifted by the vector potential A, i.e., $k \rightarrow k - A$. The latter is equivalent to assigning a time-dependent phase in the hopping elements of the tight-binding model,

$$c_n^{\dagger} c_m \to c_n^{\dagger} c_m e^{i \int_n^m A \cdot d\mathbf{r}},$$
 (5)

where n and m represent the different lattice sites with the associated creation and annihilation operators c_n^{\dagger} and c_m . Hence, an electron moving in the lattice will pick up a phase depending on the applied vector potential.

The pump is assumed to be described by a Gaussian distribution centered at t_{pump} ,

$$s(t) = A_0 e^{\frac{(t - t_{\text{pump}})^2}{2\sigma_{\text{pump}}^2}},$$
 (6)

where σ_{pump} is the width and A_0 is the magnitude. Here, we use a linearly polarized electric field $E(t) = \dot{A}$ along the a axis, with the vector potential given by $A = s(t)\omega_p^{-1}[\sin(\omega_p t)\hat{x} + \sin(\omega_p t)\hat{y}]$, where ω_p is the pump's frequency. Additionally, we neglect the relativistic magnetic field of the laser pulse as the induced corrections are small compared to electric field effects. In this case the electronic spin degree of freedom remains decoupled, and it is therefore not explicitly included in the calculations.

The transient out-of-equilibrium joint density of states [see Fig. 1(d)] is extracted from the evolution operator [49]

$$U(t,t_0) = \mathcal{T}\exp\left(-i\int_{t_0}^t dt' \tilde{H}(\mathbf{k},t')\right),\tag{7}$$

where \mathcal{T} is the time-ordered product, $t_0 \to -\infty$ is the initial time, and t is the final time. The evolution can be numerically evaluated using the Trotter decomposition

$$U(t_1, t_2) \approx U(t_1, t_1 - \Delta t)U(t_1 - \Delta t, t_1 - 2\Delta t) \cdots \times U(t_2 + \Delta t, t_2),$$
 (8)

where Δt is a small time increment chosen to provide convergence. The average energy in the presence of the pump field is given by

$$\tilde{H}(\mathbf{k},t) = \frac{1}{T} \int_{t}^{t+T} dt' \hat{H}(\mathbf{k} - \mathbf{A}(t')), \tag{9}$$

where $T=2\pi/\omega_p$ is the period of oscillation. Assuming that the latter is much shorter than the width σ_{pump} of the Gaussian pump, i.e., $T/\sigma_{\text{pump}} \ll 1$, the transient spectrum is given by the eigenvalues of the matrix

$$i \ln U(\mathbf{k}, t, t_0) = \tilde{\mathbf{d}}(t) \cdot \mathbf{\gamma}, \tag{10}$$

where

$$\tilde{\boldsymbol{d}}(t) = \left\{ \Delta, 2\tilde{K}_1(t) \sum_{\mu} \cos(k_{\mu}), \\ \times 2\tilde{K}_2(t) \cos(k_{+}) - 2K_2 \cos(k_{-}), \\ \times 2\tilde{K}_3(t) \sin(k_{+}) - 2K_3 \sin(k_{-}) \right\},$$
(11)

with $k_{\pm} = k_x \pm k_y$ being the momentum along the a or b axis and $\tilde{K}_1(t) = K_1 \int_{t_0}^t dt' J_0(s(t'))$ being the renormalized amplitude; similarly, $\tilde{K}_{2/3}(t) = K_{2/3} \int_{t_0}^t dt' J_0(2s(t'))$. Here, $J_0(z)$ is the Bessel function of the first kind. The transient out-of-equilibrium joint density of states is therefore determined by the renormalization of the hopping amplitudes $K_i \to \tilde{K}_i(t)$, i.e., of the electron's kinetic energy.

To conclude this section, we calculate the recovery rate at which the parameters $\tilde{K}_i(t)$ relax back to their equilibrium values. At times well before the pump, the hopping amplitudes are constant, i.e., $\tilde{K}_i(t \ll t_{\text{pump}}) = K_i$, representing the equilibrium state of the system. At the pump's onset, the parameters exhibit a sudden decrease and subsequently relax back to their equilibrium values with the long-time dynamics showing a slow relaxation even at times $t \gg t_{\text{pump}}$. To find the functional dependence of the relaxation time with respect to the pump's amplitude, we fit the long-time dynamics with an exponential decay,

$$\frac{\tilde{K}_i(t)}{K_i} \sim 1 - Ne^{-t/\tau},\tag{12}$$

where τ is the relaxation time and N is a normalization factor. Assuming the fitting is done at times $t \gg t_{\text{pump}}$ and the normalization is chosen such that $Ne^{-t_{\text{probe}}/\tau} = 1$, we find

$$\tau \propto \frac{1}{1 - \eta A_0^2} \propto 1 + \eta A_0^2,$$
 (13)

where η is a prefactor determined by the pump's profile and higher orders of A_0 are neglected.

III. SIGNATURES OF ULTRAFAST BAND RENORMALIZATION

We measured the transient reflectivity spectra from a single crystal of ZrSiS following photoexcitation using a visible broadband (1.75–2.25 eV) 14 fs laser pulse centered around 2 eV [see Fig. 2(a); see Secs. I and II of the Supplemental Material (SM) for material characterizations and experimental details] [50,51]. Initially, the differential reflectivity shows a negative change at high energies, along with a positive change at lower energies. After a 300–400 fs time delay, these features change to a broad positive peak with slightly negative tails on either side [see Fig. 2(b)]. For time delays > 500 fs, we observe no further change in the spectral shape within the time window of our experiments.

Using the Drude-Lorentz model, we fit the differential reflectivity spectra with Lorentzian functions [52] and find a peak at 2.06 eV which is redshifted by 113.8 meV [see Fig. 2(c)]; in the final transient state the peak recovers back to its equilibrium energy. The fitting details of the transient Drude-Lorentz reflectivity are provided in Sec. III of the SM [50]. The origin of the observed spectral features is well captured by the joint density of states [see Fig. 1(d)], where the renormalization of the kinetic energy of electrons due to out-of-equilibrium effects accounts for both the shift in resonance frequency and the renormalization of the mass in the initial transient spectra around 2 eV (see the Appendix). We note that the final spectral feature appears within 300 fs, which is the same order as the electron relaxation time

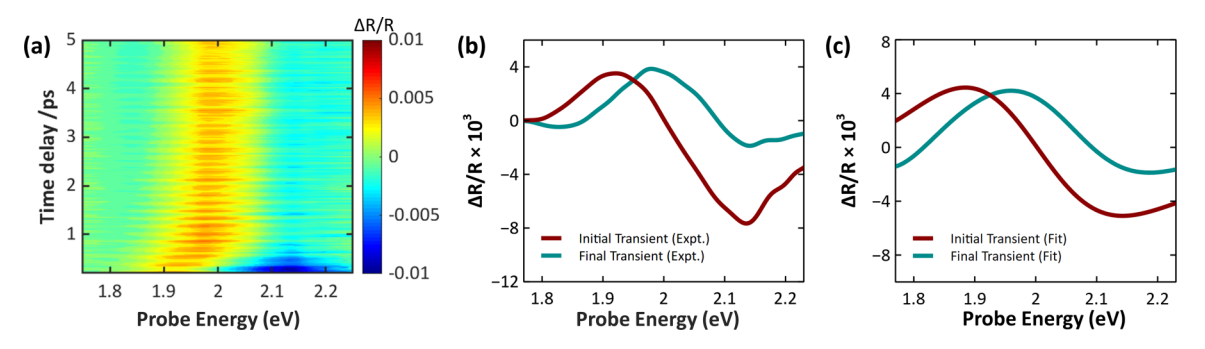


FIG. 2. (a) Transient reflectivity signal as a function of the time delay and probe energy following photoexcitation with a broadband 14-fs pulse centered around 2 eV and pump fluence of 1.24 mJ/cm². (b) Initial (200 fs) and final transient (2 ps) reflectivity spectra of ZrSiS. (c) Fitted reflectivity spectra based on the Drude-Lorentz model show good agreement with the experimental spectral line shapes. Details of the fitted parameters are provided in Sec. III of the Supplemental Material.

constant (\sim 200 fs) reported before for ZrSiS [39–41]. Therefore, the recovery of the band structure back to its equilibrium is primarily attributed to out-of-equilibrium electronic effects.

IV. FLUENCE DEPENDENCE OF BAND RENORMALIZATION EFFECTS

In order to confirm that the observed spectral features are due to ultrafast electronic effects, we performed an excitation density dependence study, where the pump fluence has been tuned between 0.3 and 1.45 mJ/cm² [see Fig. 3(a)]. Interestingly, we observe a redshift of the initial reflectivity spectra as a function of fluence and, in particular, a shift of the zero-energy crossing. In contrast, all the final spectral features look identical when they are normalized (see Sec. IV of the SM) [50]. This suggests that the ultrafast pump field affects the electronic structure only within a few hundred femtoseconds following photoexcitation. The fitted initial transient spectra, shown in Fig. 3(b), have the expected behavior with respect to fluence: we observe a shift in zero-energy crossing of the differential reflectivity, as indicated by the gray arrows. This is primarily caused by the redshift of the fitted Lorentzian peak centered at 2.06 eV, which is renormalized depending on the pump's strength [see Fig. 3(c)].

Out-of-equilibrium treatment of the tight-binding model (see Sec. II) shows that the observed spectral shift can be attributed to ultrafast processes that modify the position of the

resonant peak at \sim 2 eV according to the strength of the pump [see Fig. 1(d)]. In addition, the effective mass associated with this peak is shown to follow a quadratic behavior as a function of pump fluence (see the Appendix); in fact, quasiparticle mass enhancement was observed before in the presence of high magnetic fields [15]. Therefore, our results demonstrate the ability to modify the electronic properties of ZrSiS as a function of pump field strength, a promising avenue towards engineering novel out-of-equilibrium phases using ultrafast optical pulses.

V. ELECTRONIC RELAXATION EFFECTS

Next, we study the time evolution of the transient reflectivity signal with pump fluences of 0.30 to 1.45 mJ/cm² and extract the relaxation time by observing the decay of the negative reflectivity feature centered at 2.1 eV [see Fig. 4(a)]. The data can be well fitted with a monoexponential decay, where the fitted relaxation time ranges between 90 and 280 fs depending on the pump fluence [see Fig. 4(b)]. We note that the energy zero-cross of the differential reflectivity spectra as a function of excitation density follows a trend similar to the decay of the negative peak centered around 2.1 eV (see Sec. V of the SM) [50]. Since the recovery of the band back to its equilibrium and electronic decay are simultaneous, they must be induced by the same ultrafast process. Indeed, such relaxation dynamics are well captured within the tight-

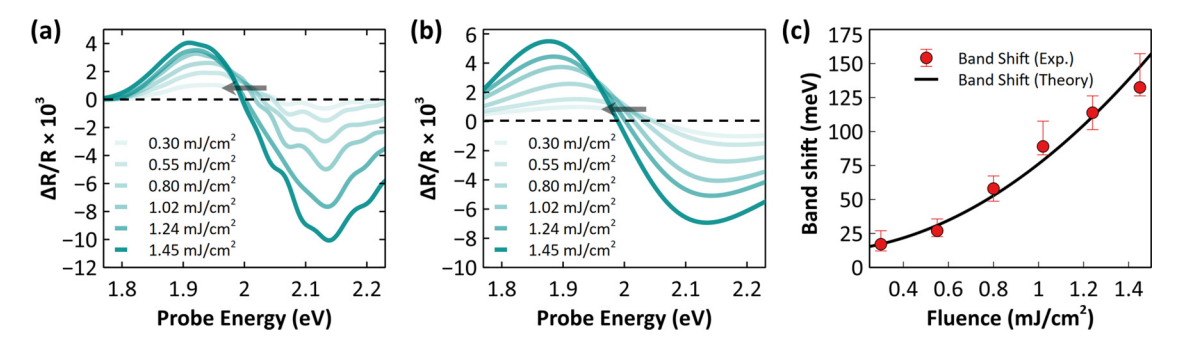


FIG. 3. (a) Fluence dependence of the initial transient spectrum. The gray arrow indicates the redshift in zero crossing energies as a function of fluence. (b) Fitted differential reflectivity spectra as a function of fluence showing the expected experimental spectral shapes and shift in zero crossing energy. (c) The shift of the fitted Lorentzian peak at 2.06 eV overlaid with the expected band shift obtained from the tight-binding model (see the Appendix).

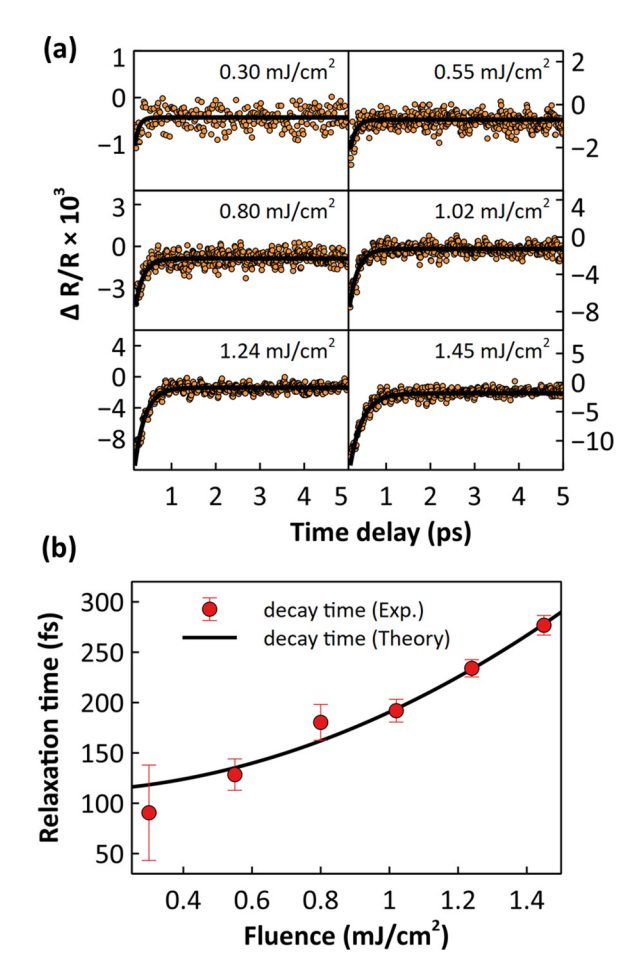


FIG. 4. (a) Fluence dependence decay of the negative reflectivity feature centered around 2.1 eV. The orange circles are the experimental data, while the solid black lines are fits with a monoexponential decay function. (b) Experimental relaxation time overlaid with the relaxation time obtained from the out-of-equilibrium treatment [see Eq. (13)].

binding model, where the electronic recovery time depends quadratically on the pump's fluence [see Eq. (13)]. Additional transient reflectively measurements with a 2 eV pump and a broadband near-infrared (NIR) (0.8–1.4 eV) probe in the NIR region show similar enhancement of the electronic relaxation time as a function of fluence (see Sec. VI of the SM) [50].

The change in electronic relaxation time in ZrSiS due to external perturbations is in contrast to previous measurements, where it was shown to be independent of several experimental parameters, including pump fluence, temperature, and magnetic fields [39,40]. Therefore, our study shows unique experimental evidence of the effect on the relaxation time in a topological semimetal using ultrashort optical excitations. While the trend in the observed relaxation rate as a function of fluence can be qualitatively described within the tight-binding model of Sec. II, we note that this behavior could also be due to the hot-phonon bottleneck effect, in which the decay of the optical phonons controls the electronic relaxation. In the following, we confirm the validity of the theory by observing the coherent phonon dynamics.

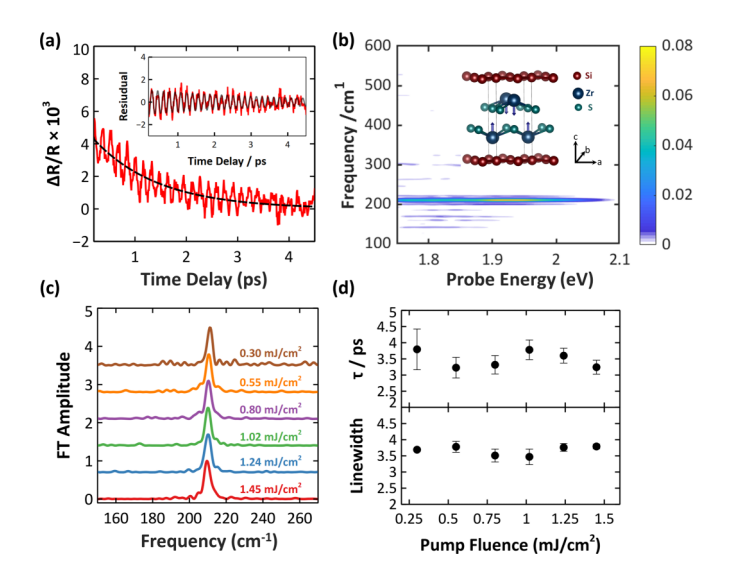


FIG. 5. (a) Line cut at 1.9 eV of the transient differential reflectivity data as a function of time delay (red line). The dashed black line is the exponential fit. The inset shows the residual with a period of 159 fs and a dephasing time constant of 3.5 ps. (b) Fourier-transformed data as a function of probe energy in the visible region showing a dominant frequency centered around 210 cm⁻¹ and the lattice vibration of ZrSiS of the A_{1g} phonon mode. (c) The Fourier-transformed frequency as a function of pump fluence. (d) Phonon dephasing rate and linewidth as a function of pump fluence.

VI. COHERENT PHONON DYNAMICS

In addition to the slow temporal change in the reflectivity spectra, we observe a fast modulation of the transient signal in the visible pump-probe measurements [$\sim 2 \text{ eV}$; see Fig. 5(a)]. This modulation originates from changes in the permittivity of the material due to atomic vibrations of the coherent Raman active phonon mode. Fourier transformation of the oscillatory signal shows a frequency at around 210 cm⁻¹ with a strong vibration amplitude between 1.75 and 2.10 eV [see Fig. 5(b)]. This mode is a symmetric A_{1g} vibration, which is an out-ofplane motion of Zr and S along the c axis of the ZrSiS lattice, as shown in the inset of Fig. 5(b) and reported previously by Raman measurements [53,54]. We attribute the observed coherent oscillation to the interband coupling between electronic modes at the Γ point and symmetric lattice vibration in ZrSiS [53]; such symmetric coherent vibrations have also been observed in other topological semimetals [55,56].

Fitting the oscillatory component with a sinusoidal wave multiplied by an exponential decay function, we extract the lifetime of the coherent phonon motion (see Sec. VII of the SM for more details) [50]. The presence of this coherent phonon is shown in Fig. 5(c) for pump fluences between 0.30 and $1.45 \, \text{mJ/cm}^2$. The observed lifetime and linewidth are independent of the fluence with an almost constant lifetime of $3.5 \pm 0.3 \, \text{ps}$ [see Fig. 5(d)]. Importantly, such lifetimes are relatively long compared to the coherent vibrations observed in the similar topological material ZrSiTe, in which the oscillations diminished within 1 ps [55]. In our case, the coherent phonon lifetime is more than an order of magnitude higher than the observed electronic relaxation time, i.e., the recovery of the bands. These observations indicate that

phononic contributions to the total change in the relaxation rate are negligible and rule out the possibility of phonon-bottleneck formation—a process by which carrier lifetime is increased based on phonon relaxation. Our results are consistent with the predicted weak electron-phonon interactions in ZrSiS [57].

VII. CONCLUSIONS

Combining an out-of-equilibrium formalism with broadband optical reflectivity measurements in the visible and NIR regions, we provided evidence of band renormalization in a topological nodal-line semimetal ZrSiS. Our fluence-dependence study showed a redshift in resonant frequencies and mass enhancement, along with an increase of the electronic relaxation timescales. These observations are inherently an ultrafast effect, as supported by theoretical and experimental analysis of the transient reflectivity, as well as by the behavior of long-lived coherent phonons. Our study demonstrates the ability of all-optical manipulation of band structure properties, including mass enhancement and electronic relaxation in ZrSiS, therefore offering a unique platform to understand light-driven photoinduced phases in topological materials.

ACKNOWLEDGMENTS

G.D.S. acknowledges support from the NSF through the Princeton Center for Complex Materials, NSF-MRSEC (Grant No. DMR-2011750). Work by I.P. and P.N. is partially supported by the Quantum Science Center (QSC), a National Quantum Information Science Research Center of the U.S. Department of Energy (DOE). I.P. is supported by the early postdoc mobility fellowship from the Swiss National Science Foundation (SNSF) under Project ID No. P2EZP2 199848. P.N. acknowledges support from a CIFAR BSE Catalyst Program that has facilitated interactions and collaborations with G.D.S. L.M.S. acknowledges support from the NSF through the Princeton Center for Complex Materials, a Materials Research Science and Engineering Center (Grant No. DMR-2011750), by Princeton University through the Princeton Catalysis Initiative, by the Gordon and Betty Moore Foundation's EPIQS initiative through Grant No. GBMF9064, by the David and Lucile Packard Foundation, and by the Sloan Foundation.

APPENDIX: LINEAR RESPONSE

Here, we calculate the response of the material under the application of a weak homogeneous external electromagnetic field representing the probe. We focus on the complex electric susceptibility $\chi(\omega)$ around the \sim 2 eV region and show that it is approximated by a Lorentzian function; that is, it is equivalent to the response of the Drude-Lorentz model [58]. Crucially, the associated resonant frequency and effective mass are shown to have a quadratic dependence on the pump's strength.

The coupling of electrons to the probe's vector potential a is introduced via the minimal coupling prescription, where the

Hamiltonian is expanded up to linear order

$$\hat{H}(\mathbf{k} - \mathbf{a}) \approx \hat{H}_0(\mathbf{k}) + a_\mu \hat{v}^\mu, \tag{A1}$$

where $\hat{H}_0(\mathbf{k})$ is the unperturbed (out-of-equilibrium) Hamiltonian and $\hat{v}^{\mu} = \partial_{k_{\mu}} \hat{H}_0(\mathbf{k})$ is the velocity matrix. The matrix elements of the electron-photon coupling are obtained by quantizing the electromagnetic field and treating it within the dipole approximation where the wavelength of the probe is much longer that the interatomic spacing. In this regime, the dielectric properties of the material can be obtained perturbatively up to a sufficiently large order; more details about the formalism can be found in standard quantum field theory textbooks [59], as well as in applications in superconductors [60,61], in charge-density wave systems [62,63], and in semiconductors [64].

Here, we consider elastic transitions where an initial state of a photon with laser frequency ω is scattered to a final state of a photon with the same frequency. The relevant leading order scattering amplitude for such a process is given by

$$\int_{\Omega',k} d\Omega' d^2 k \text{Tr} G(\Omega') \hat{v}^{\mu} G(\Omega' + \Omega) \hat{v}^{\nu}, \tag{A2}$$

where $G(\Omega) = [i\omega - \hat{H}_0(k)]^{-1}$ is the electronic Green's functions, $\Omega = (i\omega, k)$ is the four-momentum, and $\mu(\nu)$ defines the polarization of the incident (scattered) photon.

We evaluate the frequency integral in Eq. (A2) using complex analysis and the residue theorem, while the remaining momentum integrals are performed numerically. Since the polarization of the incident and scattered light is along the a axis of the crystal, the imaginary part of the complex susceptibility $\chi_{\rm Im}(\omega)$ is hence proportional to

$$\chi_{\rm Im}(\omega) \propto \sum_{\rm c.v} \int_{k} d^2 k |p_{\rm cv}^a|^2 \delta(\omega - \omega_{\rm cv}),$$
(A3)

where $p_{\rm cv}^a = \langle {\rm c}|\hat{v}^a|{\rm v}\rangle$ are the dipole matrix elements between the conduction $|{\rm c}\rangle$ and valence $|{\rm v}\rangle$ bands and $\omega_{\rm cv} = \mathcal{E}_c(\boldsymbol{k}) - \mathcal{E}_v(\boldsymbol{k})$ is their energy difference. The real part of the complex susceptibility $\chi_{\rm Re}(\omega)$ can be obtained using the Kramers-Kronig relation, leading to a Lorentzian response:

$$\chi(\omega) \propto \sum_{c,v} \int_{k} d^{2}k \frac{\omega_{p}^{2}}{\omega_{cv}^{2} - \omega^{2} - i\omega\gamma},$$
(A4)

where $\omega_p \propto |p_{\rm cv}^a|$ is the plasma frequency and $\gamma \to 0$ is the damping coefficient.

We focus on the \sim 2 eV peak of the joint density of states [see Fig. 1(d)] and note that it mainly originates from the points $k_0 = (\pm \pi/2, \pm \pi/2)$ in the Brillouin zone. Expanding the energy difference $\omega_{\rm cv}$ around $k \sim k_0 + \delta k$, where δk is a small momentum increment, we find a quadratic dispersion,

$$\omega_{\rm cv} \approx \mathcal{E}_0 + \frac{1}{2} m_{\mu\nu}^{-1} \delta \mathbf{k}^{\mu} \delta \mathbf{k}^{\nu},$$
 (A5)

with $\mathcal{E}_0 = 2\sqrt{16K_2^2 + \Delta^2}$. Similarly, the associated effective mass $m_{\mu\nu}^{-1}$ can be straightforwardly calculated using the tight-binding Hamiltonian (1); however, as the resulting expressions are cumbersome, here, we show only the off-

diagonal component,

$$m_{xy}^{-1} \propto \frac{K_1^2 K_2^2}{\mathcal{E}_0^3}.$$
 (A6)

In the out-of-equilibrium case, the hopping amplitudes are mapped to $K_i \to \tilde{K}_i(t)$, and the resonant energy becomes time dependent, $\mathcal{E}_0 \to \tilde{\mathcal{E}}_0(t)$. Using the expansion of the Bessel function $J_0(z) \approx 1 - \frac{z^2}{4}$ around small z, the functional dependence of the transient resonant frequency $\tilde{\mathcal{E}}_0(t)$ to the pump's strength A_0 is given by

$$\tilde{\mathcal{E}}_0(t) \approx \mathcal{E}_0 - \alpha(t) A_0^2,$$
 (A7)

where $\alpha(t) = \frac{64K_2^2}{\mathcal{E}_0} \int_{t_0}^t dt' \exp(\frac{(t'-t_{\mathrm{pump}})^2}{\sigma_{\mathrm{pump}}^2})$ is determined by the microscopic parameters of the model and the pump's profile s(t) [see Eq. (6)]. Similarly, the transient effective mass $\tilde{m}_{uv}^{-1}(t)$ depends quadratically on the pump's strength, i.e.,

$$\tilde{m}_{\mu\nu}^{-1}(t) \approx m_{\mu\nu}^{-1} - \beta_{\mu\nu}(t)A_0^2,$$
 (A8)

where $\beta_{\mu\nu}(t)$ is again determined by the microscopic parameters of the model and the out-of-equilibrium propagation.

- [1] L. M. Schoop, M. N. Ali, C. Straßer, A. Topp, A. Varykhalov, D. Marchenko, V. Duppel, S. S. Parkin, B. V. Lotsch, and C. R. Ast, Dirac cone protected by non-symmorphic symmetry and three-dimensional Dirac line node in ZrSiS, Nat. Commun. 7, 11696 (2016).
- [2] M. Neupane, I. Belopolski, M. M. Hosen, D. S. Sanchez, R. Sankar, M. Szlawska, S.-Y. Xu, K. Dimitri, N. Dhakal, P. Maldonado, P. M. Oppeneer, D. Kaczorowski, F. Chou, M. Z. Hasan, T. Durakiewicz, Observation of topological nodal fermion semimetal phase in ZrSiS, Phys. Rev. B 93, 201104(R) (2016).
- [3] B.-B. Fu, C.-J. Yi, T.-T. Zhang, M. Caputo, J.-Z. Ma, X. Gao, B. Q. Lv, L.-Y. Kong, Y.-B. Huang, P. Richard, M. Shi, V. N. Strocov, C. Fang, H.-M. Weng, Y.-G. Shi, T. Qian, and H. Ding, Dirac nodal surfaces and nodal lines in ZrSiS, Sci. Adv. 5, eaau6459 (2019).
- [4] X. Wang, X. Pan, M. Gao, J. Yu, J. Jiang, J. Zhang, H. Zuo, M. Zhang, Z. Wei, W. Niu, Z. Xia, X. Wan, Y. Chen, F. Song, Y. Xu, B. Wang, G. Wang, and R. Zhang, Evidence of both surface and bulk Dirac bands and anisotropic nonsaturating magnetoresistance in ZrSiS, Adv. Electron. Mater. 2, 1600228 (2016).
- [5] M. N. Ali, L. M. Schoop, C. Garg, J. M. Lippmann, E. Lara, B. Lotsch, and S. S. Parkin, Butterfly magnetoresistance, quasi-2d Dirac Fermi surface and topological phase transition in ZrSiS, Sci. Adv. 2, e1601742 (2016).
- [6] R. Singha, A. K. Pariari, B. Satpati, and P. Mandal, Large non-saturating magnetoresistance and signature of nondegenerate dirac nodes in ZrSiS, Proc. Natl. Acad. Sci. USA 114, 2468 (2017).
- [7] M. Matusiak, J. Cooper, and D. Kaczorowski, Thermoelectric quantum oscillations in ZrSiS, Nat. Commun. 8, 15219 (2017).
- [8] R. Sankar, G. Peramaiyan, I. P. Muthuselvam, C. J. Butler, K. Dimitri, M. Neupane, G. N. Rao, M.-T. Lin, and F. Chou, Crystal growth of Dirac semimetal ZrSiS with high magnetoresistance and mobility, Sci. Rep. 7, 40603 (2017).
- [9] J. Hu, Z. Tang, J. Liu, Y. Zhu, J. Wei, and Z. Mao, Nearly massless Dirac fermions and strong Zeeman splitting in the nodal-line semimetal ZrSiS probed by de Haas-van Alphen quantum oscillations, Phys. Rev. B 96, 045127 (2017).
- [10] M. B. Schilling, L. M. Schoop, B. V. Lotsch, M. Dressel, and A. V. Pronin, Flat Optical Conductivity in ZrSiS due to Two-Dimensional Dirac Bands, Phys. Rev. Lett. 119, 187401 (2017).

- [11] J. Liu and L. Balents, Correlation effects and quantum oscillations in topological nodal-loop semimetals, Phys. Rev. B 95, 075426 (2017).
- [12] N. P. Armitage, E. J. Mele, and A. Vishwanath, Weyl and Dirac semimetals in three-dimensional solids, Rev. Mod. Phys. 90, 015001 (2018).
- [13] D. Muñoz-Segovia and A. Cortijo, Many-body effects in nodalline semimetals: Correction to the optical conductivity, Phys. Rev. B 101, 205102 (2020).
- [14] Y. Shao, A. N. Rudenko, J. Hu, Z. Sun, Y. Zhu, S. Moon, A. J. Millis, S. Yuan, A. I. Lichtenstein, D. Smirnov, Z. Q. Mao, M. I. Katsnelson, and D. N. Basov, Electronic correlations in nodal-line semimetals, Nat. Phys. 16, 636 (2020).
- [15] S. Pezzini, M. Van Delft, L. Schoop, B. Lotsch, A. Carrington, M. Katsnelson, N. E. Hussey, and S. Wiedmann, Unconventional mass enhancement around the Dirac nodal loop in ZrSiS, Nat. Phys. 14, 178 (2018).
- [16] P. Narang, C. A. Garcia, and C. Felser, The topology of electronic band structures, Nat. Mater. 20, 293 (2021).
- [17] D. M. Juraschek and P. Narang, Magnetic control in the terahertz, Science **374**, 1555 (2021).
- [18] A. S. Disa, T. F. Nova, and A. Cavalleri, Engineering crystal structures with light, Nat. Phys. 17, 1087 (2021).
- [19] A. de la Torre, D. M. Kennes, M. Claassen, S. Gerber, J. W. McIver, and M. A. Sentef, Colloquium: Nonthermal pathways to ultrafast control in quantum materials, Rev. Mod. Phys. 93, 041002 (2021).
- [20] Y. Wang, H. Steinberg, P. Jarillo-Herrero, and N. Gedik, Observation of Floquet-Bloch states on the surface of a topological insulator, Science 342, 453 (2013).
- [21] M. Schultze, E. M. Bothschafter, A. Sommer, S. Holzner, W. Schweinberger, M. Fiess, M. Hofstetter, R. Kienberger, V. Apalkov, V. S. Yakovlev, M. I. Stockman, and F. Krausz, Controlling dielectrics with the electric field of light, Nature (London) 493, 75 (2013).
- [22] J. Orenstein, Quantum materials, Phys. Today 65(9), 44 (2012).
- [23] C. P. Weber, Ultrafast investigation and control of Dirac and Weyl semimetals, J. Appl. Phys. **129**, 070901 (2021).
- [24] M. J. Rosker, M. Dantus, and A. H. Zewail, Femtosecond clocking of the chemical bond, Science 241, 1200 (1988).
- [25] L. Bucciantini, S. Roy, S. Kitamura, and T. Oka, Emergent Weyl nodes and Fermi arcs in a Floquet Weyl semimetal, Phys. Rev. B 96, 041126(R) (2017).

- [26] H. Hübener, M. A. Sentef, U. De Giovannini, A. F. Kemper, and A. Rubio, Creating stable Floquet-Weyl semimetals by laser-driving of 3D Dirac materials, Nat. Commun. 8, 13940 (2017).
- [27] S. Ebihara, K. Fukushima, and T. Oka, Chiral pumping effect induced by rotating electric fields, Phys. Rev. B 93, 155107 (2016).
- [28] C.-K. Chan, Y.-T. Oh, J. H. Han, and P. A. Lee, Type-II Weyl cone transitions in driven semimetals, Phys. Rev. B **94**, 121106(R) (2016).
- [29] Z. Yan and Z. Wang, Tunable Weyl Points in Periodically Driven Nodal Line Semimetals, Phys. Rev. Lett. 117, 087402 (2016).
- [30] O. V. Kibis, K. Dini, I. V. Iorsh, and I. A. Shelykh, All-optical band engineering of gapped Dirac materials, Phys. Rev. B 95, 125401 (2017).
- [31] C. Zhu, F. Wang, Y. Meng, X. Yuan, F. Xiu, H. Luo, Y. Wang, J. Li, X. Lv, L. He, Y. Xu, J. Liu, C. Zhang, Y. Shi, R. Zhang, and S. Zhu, A robust and tuneable mid-infrared optical switch enabled by bulk Dirac fermions, Nat. Commun. 8, 14111 (2017).
- [32] M. Yang, J. Wang, Y. Yang, Q. Zhang, C. Ji, G. Wu, Y. Su, J. Gou, Z. Wu, K. Yuan, F. Xiu, and Y. Jiang, Ultraviolet to long-wave infrared photodetectors based on a three-dimensional Dirac semimetal/organic thin film heterojunction, J. Phys. Chem. Lett. 10, 3914 (2019).
- [33] J. Liu, F. Xia, D. Xiao, F. J. Garcia de Abajo, and D. Sun, Semimetals for high-performance photodetection, Nat. Mater. 19, 830 (2020).
- [34] B. Cheng, N. Kanda, T. N. Ikeda, T. Matsuda, P. Xia, T. Schumann, S. Stemmer, J. Itatani, N. P. Armitage, and R. Matsunaga, Efficient Terahertz Harmonic Generation with Coherent Acceleration of Electrons in the Dirac Semimetal Cd₃As₂, Phys. Rev. Lett. 124, 117402 (2020).
- [35] S. Almutairi, Q. Chen, M. Tokman, and A. Belyanin, Four-wave mixing in Weyl semimetals, Phys. Rev. B 101, 235156 (2020).
- [36] Y. Meng, C. Zhu, Y. Li, X. Yuan, F. Xiu, Y. Shi, Y. Xu, and F. Wang, Three-dimensional Dirac semimetal thin-film absorber for broadband pulse generation in the near-infrared, Opt. Lett. 43, 1503 (2018).
- [37] C.-K. Chan, N. H. Lindner, G. Refael, and P. A. Lee, Photocurrents in Weyl semimetals, Phys. Rev. B 95, 041104(R) (2017).
- [38] L. M. Schoop, F. Pielnhofer, and B. V. Lotsch, Chemical principles of topological semimetals, Chem. Mater. **30**, 3155 (2018).
- [39] C. P. Weber, B. S. Berggren, M. G. Masten, T. C. Ogloza, S. Deckoff-Jones, J. Madeo, M. K. L. Man, K. M. Dani, L. Zhao, G. Chen, J. Liu, Z. Mao, L. M. Schoop, B. V. Lotsch, S. S. P. Parkin, and M. Ali, Similar ultrafast dynamics of several dissimilar Dirac and Weyl semimetals, J. Appl. Phys. 122, 223102 (2017).
- [40] R. J. Kirby, A. Ferrenti, C. Weinberg, S. Klemenz, M. Oudah, S. Lei, C. P. Weber, D. Fausti, G. D. Scholes, and L. M. Schoop, Transient Drude response dominates near-infrared pump–probe reflectivity in nodal-line semimetals ZrSiS and ZrSiSe, J. Phys. Chem. Lett. 11, 6105 (2020).
- [41] C. P. Weber, L. M. Schoop, S. S. P. Parkin, R. C. Newby, A. Nateprov, B. Lotsch, B. M. K. Mariserla, J. M. Kim, K. M. Dani, H. A. Bechtel, E. Arushanov, and M. Ali, Directly photoexcited Dirac and Weyl fermions in ZrSiSe and NbAs, Appl. Phys. Lett. 113, 221906 (2018).

- [42] G. Gatti, A. Crepaldi, M. Puppin, N. Tancogne-Dejean, L. Xian, U. De Giovannini, S. Roth, S. Polishchuk, P. Bugnon, A. Magrez, H. Berger, F. Frassetto, L. Poletto, L. Moreschini, S. Moser, A. Bostwick, E. Rotenberg, A. Rubio, M. Chergui, and M. Grion, Light-Induced Renormalization of the Dirac Quasiparticles in the Nodal-Line Semimetal ZrSiSe, Phys. Rev. Lett. 125, 076401 (2020).
- [43] N. Nilforoushan, M. Casula, M. Caputo, E. Papalazarou, J. Caillaux, Z. Chen, L. Perfetti, A. Amaricci, D. Santos-Cottin, Y. Klein, A. Gauzzi, and M. Marsi, Photoinduced renormalization and electronic screening of quasi-two-dimensional Dirac states in BaNiS₂, Phys. Rev. Res. 2, 043397 (2020).
- [44] A. N. Rudenko, E. A. Stepanov, A. I. Lichtenstein, and M. I. Katsnelson, Excitonic Instability and Pseudogap Formation in Nodal Line Semimetal ZrSiS, Phys. Rev. Lett. 120, 216401 (2018).
- [45] D. Xiao, J. Shi, and Q. Niu, Berry Phase Correction to Electron Density of States in Solids, Phys. Rev. Lett. 95, 137204 (2005).
- [46] C. Duval, Z. Horváth, P. A. Horvathy, L. Martina, and P. Stichel, Berry phase correction to electron density in solids and "exotic" dynamics, Mod. Phys. Lett. B 20, 373 (2006).
- [47] K. Yu. Bliokh, On the Hamiltonian nature of semiclassical equations of motion in the presence of an electromagnetic field and Berry curvature. Phys. Lett. A 351, 123 (2006).
- [48] P. Gosselin, F. Ménas, A. Bérard, and H. Mohrbach, Semiclassical dynamics of electrons in magnetic Bloch bands: A Hamiltonian approach, Europhys. Lett. **76**, 651 (2006).
- [49] J. K. Freericks, H. R. Krishnamurthy, and T. Pruschke, Theoretical Description of Time-Resolved Photoemission Spectroscopy: Application to Pump-Probe Experiments, Phys. Rev. Lett. 102, 136401 (2009).
- [50] See Supplemental Material at http://link.aps.org/supplemental/ 10.1103/PhysRevB.106.134303 for experimental details, optical setups, and Lorentz-Drude fittings.
- [51] S. D. McClure, D. B. Turner, P. C. Arpin, T. Mirkovic, and G. D. Scholes, Coherent oscillations in the pc577 cryptophyte antenna occur in the excited electronic state, J. Phys. Chem. B 118, 1296 (2014).
- [52] A. Kuzmenko, Kramers–Kronig constrained variational analysis of optical spectra, Rev. Sci. Instrum. **76**, 083108 (2005).
- [53] W. Zhou, H. Gao, J. Zhang, R. Fang, H. Song, T. Hu, A. Stroppa, L. Li, X. Wang, S. Ruan, and W. Ren, Lattice dynamics of Dirac node-line semimetal ZrSiS, Phys. Rev. B 96, 064103 (2017).
- [54] R. Singha, S. Samanta, S. Chatterjee, A. Pariari, D. Majumdar, B. Satpati, L. Wang, A. Singha, and P. Mandal, Probing lattice dynamics and electron-phonon coupling in the topological nodal-line semimetal ZrSiS, Phys. Rev. B 97, 094112 (2018).
- [55] R. J. Kirby, L. Muechler, S. Klemenz, C. Weinberg, A. Ferrenti, M. Oudah, D. Fausti, G. D. Scholes, and L. M. Schoop, Signature of an ultrafast photoinduced Lifshitz transition in the nodal-line semimetal ZrSiTe, Phys. Rev. B 103, 205138 (2021).
- [56] C. P. Weber, M. G. Masten, T. C. Ogloza, B. S. Berggren, M. K. L. Man, K. M. Dani, J. Liu, Z. Mao, D. D. Klug, A. A. Adeleke, and Y. Yao, Using coherent phonons for ultrafast control of the Dirac node of SrMnSb₂, Phys. Rev. B 98, 155115 (2018).
- [57] A. N. Rudenko and S. Yuan, Electron-phonon interaction and zero-field charge carrier transport in the nodal-line semimetal ZrSiS, Phys. Rev. B 101, 115127 (2020).

- [58] M. Cardona and Y. Y. Peter, *Fundamentals of semiconductors* (Springer-Verlag, Berlin Heidelberg, 2005).
- [59] M. E. Peskin and D. V. Schroeder, *An Introduction to Quantum Field Theory* (Westview, Reading, USA, 1995).
- [60] E. Dagotto, Correlated electrons in high-temperature superconductors, Rev. Mod. Phys. **66**, 763 (1994).
- [61] B. Valenzuela, M. J. Calderón, G. León, and E. Bascones, Optical conductivity and Raman scattering of iron superconductors, Phys. Rev. B 87, 075136 (2013).
- [62] B. Horovitz, Z. Vardeny, E. Ehrenfreund, and O. Brafman, Raman scattering from charge-density waves and application to polyacetylene, J. Phys. C 19, 7291 (1986).
- [63] M. V. Klein, Theory of Raman scattering from charge-densitywave phonons, Phys. Rev. B 25, 7192 (1982).
- [64] S. Reichardt and L. Wirtz, Raman spectroscopy of graphene, in *Optical Properties of Graphene* (World Scientific, Singapore, 2017), pp. 85–132.